Monthly Notices
of the
ROYAL ASTRONOMICAL SOCIETY

MNRAS **446,** 411–427 (2015) doi:10.1093/mnras/stu2067

Mass and period limits on the ringed companion transiting the young star J1407

M. A. Kenworthy,[1⋆] S. Lacour,[2] A. Kraus,[3] A. H. M. J. Triaud,[4,5†] E. E. Mamajek,[6] E. L. Scott,[6] D. Ségransan,[5] M. Ireland,[7] F.-J. Hambsch,[8] D. E. Reichart,[9] J. B. Haislip,[9] A. P. LaCluyze,[9] J. P. Moore[9] and N. R. Frank[9]

[1]*Leiden Observatory, Leiden University, PO Box 9513, NL-2300 RA Leiden, the Netherlands*
[2]*LESIA, CNRS/UMR-8109, Observatoire de Paris, UPMC, Université Paris Diderot, 5 place Jules Janssen, F-92195 Meudon, France*
[3]*Institute for Astronomy, University of Hawaii, 2680 Woodlawn Drive, Honolulu, HI 96822, USA*
[4]*Kavli Institute for Astrophysics & Space Research, Massachusetts Institute of Technology, Cambridge, MA 02139, USA*
[5]*Observatoire Astronomique de l'Université de Genève, Chemin des Maillettes, 51, CH-1290 Sauverny, Switzerland*
[6]*Department of Physics and Astronomy, University of Rochester, Rochester, NY 14627-0171, USA*
[7]*Research School of Astronomy and Astrophysics, Mt Stromlo Observatory, Cotter Rd, Weston, ACT 2611, Australia*
[8]*Center for Backyard Astrophysics (Antwerp), American Association of Variable Star Observers (AAVSO), Vereniging Voor Sterrenkunde (VVS), Andromeda Observatory, Oude Bleken 12, B-2400 Mol, Belgium*
[9]*Department of Physics and Astronomy, University of North Carolina at Chapel Hill, Campus Box 3255, Chapel Hill, NC 27599, USA*

Accepted 2014 October 1. Received 2014 October 1; in original form 2014 July 8

ABSTRACT

The young (∼16 Myr) pre-main-sequence star in Sco–Cen 1SWASP J140747.93−394542.6, hereafter referred to as J1407, underwent a deep eclipse in 2007 April, bracketed by several shallower eclipses in the surrounding 54 d. This has been interpreted as the first detection of an eclipsing ring system circling a substellar object (dubbed J1407b). We report on a search for this companion with Sparse Aperture Mask imaging and direct imaging with both the UT4 VLT and Keck telescopes. Radial velocity measurements of J1407 provide additional constraints on J1407b and on short period companions to the central star. Follow-up photometric monitoring using the Panchromatic Robotic Optical Monitoring and Polarimetry Telescopes (PROMPT)-4 and ROAD observatories during 2012–2014 has not yielded any additional eclipses. Large regions of mass–period space are ruled out for the companion. For circular orbits the companion period is constrained to the range 3.5–13.8 yr ($a \simeq 2.2$–5.6 au), and stellar masses ($>80 M_{\rm Jup}$) are ruled out at 3σ significance over these periods. The complex ring system appears to occupy more than 0.15 of its Hill radius, much larger than its Roche radius and suggesting a ring structure in transition. Further, we demonstrate that the radial velocity of J1407 is consistent with membership in the Upper Cen–Lup subgroup of the Sco–Cen association, and constraints on the rotation period and projected rotational velocity of J1407 are consistent with a stellar inclination of $i_\star \simeq 68^\circ \pm 10^\circ$.

Key words: planets and satellites: formation – planets and satellites: rings – binaries: eclipsing – stars: individual: 1SWASP J140747.93−394542.6 (ASAS J140748−3945.7) – planetary systems.

1 INTRODUCTION

An otherwise unremarkable pre-main-sequence star in the nearby Sco–Cen OB Association, 1SWASP J140747.93−394542.6 (hereafter J1407) suddenly exhibited an extremely long, deep, and complex eclipse in mid-2007, lasting 54 d and achieving a maximum depth of >3 mag (Mamajek et al. 2012). This eclipse morphology is markedly different when compared with a typical eclipsing binary or exoplanet, but is very reminiscent of the light curves for stars such as ϵ Aurigae (Guinan & Dewarf 2002; Kloppenborg et al. 2010; Chadima et al. 2011), KH 15D (Winn et al. 2006), EE Cep (Mikolajewski & Graczyk 1999; Graczyk et al. 2003; Mikolajewski et al. 2005) that are periodically occulted by extended objects. Given its youth, J1407 is most likely being eclipsed by a low-mass object hosting a disc with significant substructure composed of thin dust debris belts, or 'rings'. There is no evidence of flux from this

⋆E-mail: kenworthy@strw.leidenuniv.nl
†Fellow of the Swiss National Science Foundation.

companion, indicating that it is a very low mass star, brown dwarf, or perhaps even a gas giant planet (Mamajek et al. 2012).

J1407 was identified as a probable young star by virtue of its X-ray emission, a proper motion consistent with the motion of Sco–Cen, and its CMD position on the Sco–Cen stellar sequence (Mamajek et al. 2012; Pecaut 2013). Spectroscopic follow-up using the CTIO 1.5 m telescope confirmed the object to be a young, Li-rich K5 star, lacking any accretion indicators (Mamajek et al. 2012) or infrared excess at short (2MASS; Skrutskie et al. 2006) and long wavelengths (WISE photometry; Wright et al. 2010). The star therefore appears to be a weak-lined T Tauri star, not hosting its own circumstellar disc, and is a young (∼16 Myr) solar analogue ($M \sim 0.9\,M_{\odot}$).

This star was observed by the Super Wide Angle Search for Planets (SuperWASP) survey (Pollacco et al. 2006; Butters et al. 2010) in 2007 as part of their wide-field search for transiting exoplanets. Simultaneously and independently, the field was also observed at much lower cadence by the All Sky Automated Survey (ASAS; Pojmanski 2002). Both surveys revealed a remarkably long, deep, and complex eclipse event centred on UT 2007 April 29. At least five multiday dimming events of >0.5 mag were identified, with a >3.3 mag deep eclipse bracketed by two pairs of ∼1 mag eclipses symmetrically occurring ±12 d and ±26 d before and after. Hence, significant dimming of the star was taking place on and off over at least a ∼54 d period in 2007, and a strong >3 mag dimming event occurring over a ∼12 d span. Mamajek et al. (2012) hypothesized that a complex ring system circling an unseen lower mass companion passed in front of J1407 over the span of several weeks.

The WASP pipeline is optimized for identifying transiting planets, which typically produce trough-like eclipses of 1 per cent depth lasting a few hours. In the case of J1407, it was located in the corner of the field of view of three of the WASP-South cameras, and the photometry from different cameras showed systematic relative offsets of up to 0.3 mag. A custom reduction pipeline was created for J1407 and these systematic effects, along with the rotational variability, were removed to produce a cleaned light curve (van Werkhoven, Kenworthy & Mamajek 2014).

For orbital periods of 20–100 yr ($a > 7$ au), the projected separation is in the range of ∼60 mas. Given the likely faintness of the companion, it falls well below the angular resolving limits of traditional adaptive optics imaging on 8–10 m class telescopes. Sparse aperture masking (SAM) or Non-Redundant Masking (NRM) delivers an increase in resolution within the Airy disc diffraction limit (e.g. Nakajima et al. 1989; Tuthill et al. 2006), and is now a well-established means of achieving the full diffraction limit of a single telescope (e.g. Ireland et al. 2008; Kraus & Hillenbrand 2009; Lacour et al. 2011).

Predicting when the next eclipse will happen is paramount to planning an extensive and detailed observing campaign. This object offers an unprecedented opportunity to spatially and spectrally resolve a disc with ring-like structure orbiting a likely substellar object at age ∼16 Myr. In this paper, we report on our search for the proposed companion J1407b. In Section 2, we describe the observations and data reduction. We do not detect any companion to J1407 with interferometric or direct imaging, and high spectral resolution radial velocity (RV) measurements show no companion in the system. Using these constraints, we provide a simple model for circular and elliptical orbital solutions (Section 4) and show which orbital periods can be ruled out. We discuss the consequences of these observations for the J1407 system in Section 5.

2 OBSERVATIONS AND DATA REDUCTION

J1407 has been observed with several different instruments, all providing different constraints on companions in the system. In the first three sections, we present interferometric and direct imaging observations from the VLT and Keck. The next two sections detail RV measurements from MIKE on the Magellan telescope and CORALIE on the Euler telescope. The last sections detail photometric monitoring with the Panchromatic Robotic Optical Monitoring and Polarimetry Telescopes (PROMPT)-4 and the Remote Observatory Atacama Desert (ROAD) observatory.

2.1 SAM at the VLT

Sparse Aperture Masking takes the filled single dish telescope pupil and selects several smaller apertures from it. The locations of these apertures are chosen so that all pairwise combinations form a set of unique baselines. The resultant point spread function (PSF) in the focal plane of the science camera then encodes spatial information about the science target that can be reconstructed to form a model of the source. Slow changing aberrations within the telescope and science instrument can be calibrated out by interleaving science observations with those of a similar brightness reference source. The outer size is set by the shortest baseline between two apertures and an inner size set by the interferometric limit ($\lambda/2D$). Complete baseline coverage is obtained thanks to the rotation of the target along the parallactic angle during the observation. Although there is a penalty in reduced throughput, SAM imaging can reach imaging scales that are not easily attainable with classical adaptive optics assisted direct imaging. This interferometric method is also referred to as NRM and this term can be interchangeably used with SAM imaging. We use SAM for the rest of this paper. For both Keck and VLT, maximizing throughput using the sparsest mask with the largest apertures is almost always better for detecting point source companions than maximizing baselines (using a denser mask with smaller apertures). As the target star is relatively faint for SAM imaging and the secondary companion is expected to be a point source, choosing as few baselines as possible helps optimize signal to noise(S/N).

Several SAM modes with different aperture configurations are implemented with the NaCo system at the VLT (Lacour et al. 2011). Observations were taken with VLT NaCo on UT 2013 March 27 and 28. We use the '7-hole' mask for maximum throughput. The conditions for both nights were photometric with no cloud cover. The VLT seeing monitor reported 0.5–0.9 arcsec seeing on both nights, with coherence times of 4 ms over the whole observing run (see Table 1). J1407 has a visual magnitude $V = 12.31 \pm 0.03$ (Mamajek et al. 2012) and $K_s = 9.26 \pm 0.02$ (2MASS; Skrutskie et al. 2006). The properties of the star J1407 are detailed in van Werkhoven et al. (2014) and we use them for the rest of this paper – the distance is taken to be 133 ± 13 pc with an age of 16 Myr. We use the 90 per cent IR dichroic and the infrared wavefront sensor (WFS) so that the target star is used as a natural guide star for the adaptive optics system.

The telescope optics and instrument have a time-varying optical aberration associated with them, and so SAM observations of the science (SCI) target require known single star observations (CAL observations) to be interspersed between them. Moving between the science and calibration stars incurs an observing overhead, and so a balance must be found between remaining on the science target and the change in telescope aberrations that cannot be removed by sparse calibration observations. The time between

Table 1. Observing log for the SAM imaging. All data are taken with the K_s filter and '7-hole' SAM.

Star	UT start	DIT[a] (s)	N_{DIT}[b]	Pointing[c] offsets	Seeing[d] (arcsec)	τ_0[e] (ms)
J1407	2013-03-27 05:01:41	10	5	8	1.16	2.53
2M1407−3941	2013-03-27 05:15:51	5	10	8	0.82	3.44
J1407	2013-03-27 05:29:06	10	5	8	0.74	3.86
2M1407−3948	2013-03-27 05:44:38	7	7	8	0.73	3.83
J1407	2013-03-27 05:56:37	10	5	8	0.66	4.21
2M1407−3941	2013-03-27 06:06:54	5	10	8	0.76	3.63
J1407	2013-03-27 06:18:25	10	5	8	0.80	3.48
2M1407−3948	2013-03-27 06:29:28	7	7	8	0.96	2.82
J1407	2013-03-27 06:42:50	10	5	8	0.86	3.29
2M1407−3941	2013-03-27 06:55:34	5	10	8	0.70	3.99
J1407	2013-03-27 07:06:17	10	5	8	0.75	3.90
2M1407−3948	2013-03-27 07:17:51	7	7	8	0.74	3.84
J1407	2013-03-27 07:28:52	10	5	8	0.71	3.99
2M1407−3941	2013-03-27 07:39:26	5	10	8	0.61	4.65
J1407	2013-03-27 07:50:22	10	5	8	0.62	4.59
2M1407−3948	2013-03-27 08:01:02	7	7	8	0.61	4.66
J1407	2013-03-27 08:11:37	10	5	8	0.64	4.55
2M1407−3941	2013-03-27 08:22:56	5	10	8	0.65	4.55
J1407	2013-03-27 08:40:11	12	4	8	1.03	2.86
2M1407−3948	2013-03-27 08:51:28	7	7	8	0.84	3.63
J1407	2013-03-28 04:25:45	10	30	4	0.70	3.25
2M1407−3941	2013-03-28 04:50:02	10	30	4	0.85	2.94
J1407	2013-03-28 05:13:54	10	30	4	0.69	3.59
2M1407−3941	2013-03-28 05:38:07	10	30	4	0.64	3.74
J1407	2013-03-28 06:14:46	10	30	4	0.65	3.62
2M1407−3941	2013-03-28 06:39:22	10	15	4	0.77	3.19
J1407	2013-03-28 06:52:45	10	30	4	0.73	2.81
2M1407−3948	2013-03-28 07:18:27	10	21	4	0.67	3.50
J1407	2013-03-28 07:36:47	10	30	4	0.58	3.78
2M1407−3941	2013-03-28 08:01:13	10	15	4	0.68	3.83
J1407	2013-03-28 08:15:36	10	30	4	0.81	2.87
2M1407−3948	2013-03-28 08:40:42	10	21	4	0.69	3.18
J1407	2013-03-28 09:00:14	10	30	4	0.60	3.88
2M1407−3941	2013-03-28 09:24:51	10	15	4	0.58	3.82
J1407	2013-03-28 09:37:56	10	30	4	0.62	3.55
2M1407−3948	2013-03-28 10:01:58	10	21	4	0.91	2.41

[a]DIT: detector integration time (single frame exposure time).
[b]N_{DIT}: number of detector integration times.
[c]Number of pointing positions on the detector.
[d]Mean DIMM seeing [$\lambda = 500$ nm].
[e]Average coherence time as calculated by the AO system.

Table 2. Properties of stars observed.

Object	K_s (mag)	Total integration time (s)
2MASS J14074792−3945427 (SCI)	9.257 ± 0.020	13 584
2MASS J14074401−3941140 (CAL)	8.345 ± 0.026	6200
2MASS J14072080−3948550 (CAL)	8.874 ± 0.021	4480

SCI and CAL observations is determined from previous observing experience to be of the order of a few minutes. Observations are alternated between J1407 (SCI) and two calibration stars chosen from previous SAM observing runs 2MASS J14074401−3941140 and 2MASS J14072080−3948550. Even though these stars were used as calibrators in other previous observations by us, there is always the chance that a calibrator is a long period binary and that the data is rendered uncalibratable. To mitigate this, two calibration stars with similar magnitudes and colours to the science target are chosen. Between the first and second night it was discovered that the first night observations were photon noise limited and not calibration noise limited, and so the dwell time between SCI and CAL observations was increased from 50–300 s. Data for J1407 were taken in an eight-point dither pattern on the first night, and subsequently in a four-point dither pattern on the second night, resulting in an increase in S/N ratio. The observing parameters of both J1407 and the calibration stars are detailed in Table 2.

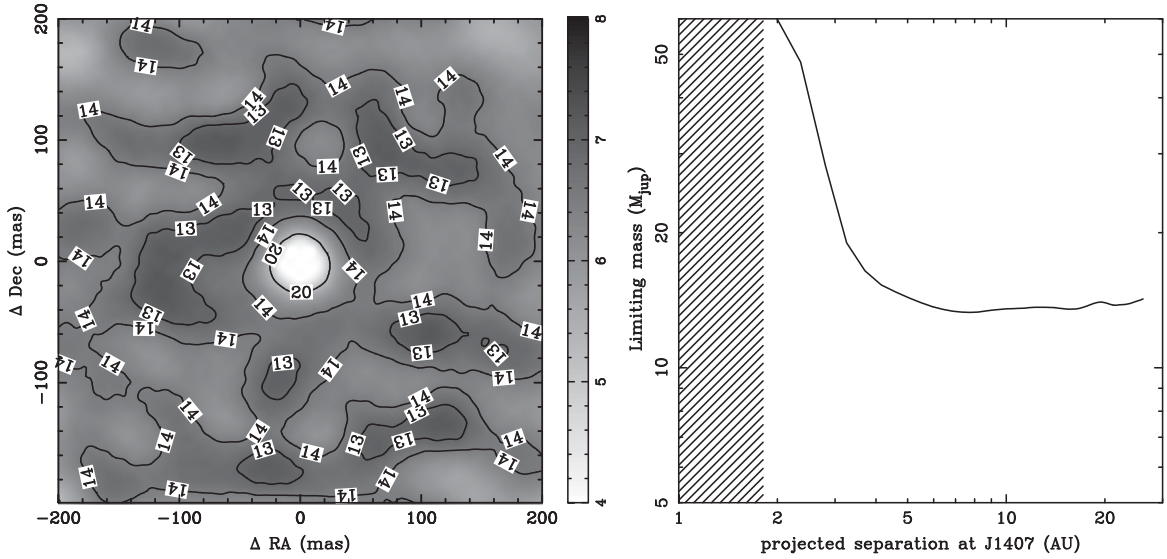

Figure 1. Sensitivity map of J1407 from SAM imaging at the VLT. Left-hand panel: the star is at the centre of the image, the grey-scale and side bar indicate the sensitivity in delta K_s magnitudes for a 3σ point source detection. The contours indicate the associated upper mass limits in units of Jupiter masses ($M_{\rm Jup}$) estimated from the K_s photometry and models from Allard, Homeier & Freytag (2012a). North is up and east to the left. Right-hand panel: azimuthally averaged sensitivity map. The hashed region indicates circular orbital periods of $P < 850$ d that are ruled out by Mamajek et al. (2012).

The VLT data were reduced by fitting the diffraction pattern on each one of the detector images. Each image of a data cube consists in a number of fringes of given spatial frequency (proportional to the baseline vector between each pair of holes), and given phase. The procedure is explained in more details in Lacour et al. (2011), but roughly, the phases and amplitudes are used to derive the uncalibrated visibilities, which are in turn used to compute the bispectrum. The data reduction is done similarly on the Keck data, but with a notable difference that the visibility measurements are obtained by fast Fourier transform. The bispectrum is then co-added over all the frames of one data cube, of which the argument is taken as the closure phase. The final step for the J1407 data is to correct for biases in the closure-phase measurement, by subtracting the closure-phase values of the two calibrators closest in time.

The sensitivity map is obtained by the mean of calculating the χ^2 between the data and a binary model. We used the binary model from Le Bouquin & Absil (2012) to compute synthetic closure phases:

$$CP = \arg[(1 + \rho e^{i\alpha_{ij}})(1 + \rho e^{i\alpha_{jk}})(1 + \rho e^{i\alpha_{ki}})], \quad (1)$$

where ρ is the flux ratio between the two stars, and α_{ij} is a function of the baseline vector between to holes i and j, but also a function of the separation between the primary and the secondary stars (Δ):

$$\alpha_{ij} = 2\pi \boldsymbol{B}_{ij} \cdot \boldsymbol{\Delta}/\lambda. \quad (2)$$

The χ^2 is then computed over a three-dimensional grid (ρ,$\boldsymbol{\Delta}$), and normalized so the χ^2 of a non-detection ($\Delta = 0$) is equal to the number of closure-phase measurements. Finally, for any separation $\boldsymbol{\Delta}$, the sensitivity limit is obtained by taking the ρ value where the χ^2 is equal the number of closure phases plus 25. Note that this $\chi^2 + 25$ limit corresponds to a 3.3σ and not a 5σ sensitivity limit because of the covariance of the closure phases (for a 7-hole mask, there are 15 independent quantities instead of 35). We conservatively adopt all subsequent sensitivity maps as being 3σ point source detection limited.

The results of the observations are shown in Fig. 1. We do not detect any point sources within the 400 mas region surrounding J1407. Due to the combination of observing conditions and sky rotation, the sensitivity for a 3σ detection varies by 1 mag at a given radius. The sensitivity map is shown in ΔK_s magnitudes as a grey-scale image. We use BT-SETTL models without irradiation and Caffau solar abundances (Caffau et al. 2011; Allard et al. 2012a) to estimate the limiting companion mass from the delta K_s magnitude, the distance to the star, and its apparent magnitude. The resultant mass limits are shown as the contour map in Fig. 1 in units of Jupiter mass ($M_{\rm Jup}$). It can be seen that masses below $13M_{\rm Jup}$ are reached in several regions around J1407, rising to $20M_{\rm Jup}$ for radii of 28 mas (3 au) and smaller.

2.2 SAM at Keck

We observed J1407 on UT 2012 April 4 using the Keck-II 10 m telescope with natural guide star adaptive optics. All observations were conducted with the facility AO imager, Near Infrared Camera 2 (NIRC2), which has aperture masks installed in the cold filter wheel near the pupil stop. We used a 9-hole aperture mask, which yields 28 independent baseline triangles about which closure phases are measured. All SAM observations operate in a subarray mode of the narrow camera, and we conducted our observations using the broad-band K' filter. The observing sequence consisted of one set of 21 integrations of 20 s for J1407, preceded and followed by similar observations of independent calibrator stars. We summarize these observations in Table 3.

The analysis for the SAM data was identical to that used in previous papers (e.g. Ireland & Kraus 2008; Kraus et al. 2008,

Table 3. Keck-II observations.

Object	Number of frames	Notes
PDS 70	21	Calibrator
J1407	21	
14213051	13	Binary ($\rho = 1$ arcsec, $\Delta K = 0$)
14085608	21	Binary ($\rho = 230$ mas, $\Delta K = 2$)
MML 40	12	Calibrator

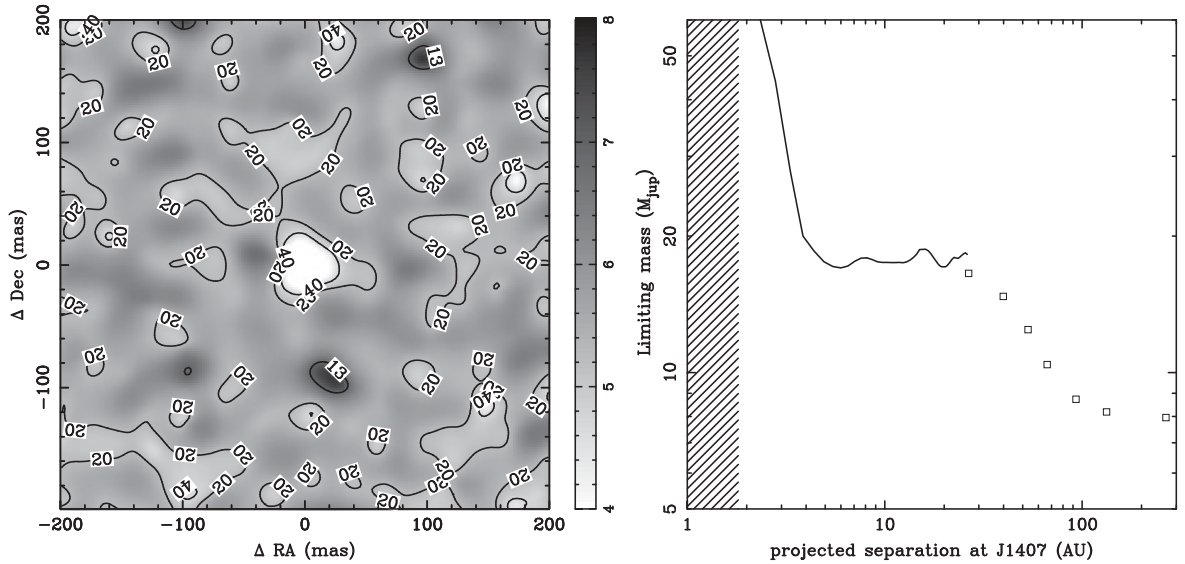

Figure 2. Sensitivity map of J1407 from SAM imaging at Keck. Left-hand panel: the star is at the centre of the image, the grey-scale and side bar indicate the sensitivity in delta K_s magnitudes for a 3σ point source detection. The contours indicate the associated upper mass limits in units of Jupiter masses (M_{Jup}) estimated from the K_s photometry and models from Allard et al. (2012a). North is up and east to the left. Right-hand panel: Azimuthally averaged sensitivity map. The hashed region indicates circular orbital periods of $P < 850$ d that are ruled out by Mamajek et al. (2012). The open squares are the sensitivity limits from direct imaging observations with Keck.

2011), combined with the new calibration technique described in Kraus & Ireland (2012). To summarize, the images were flat fielded and bad pixels were removed by interpolating between neighbouring pixels. The image was then multiplied by a super-Gaussian window function of the form $\exp(-ar^4)$, with r the radius in pixels from the centre of the interferogram. A two-dimensional Fourier transform was then made of each exposure in a visit, and this Fourier transform was point sampled at the positions corresponding to the baseline vectors in the aperture mask. For each visit we then computed the vector of mean uncalibrated closure phases and the standard error of the mean. Finally, we calibrated the closure phases for each visit using an optimal linear combination of the calibrators observed in the same sequence of events. Our analysis found no statistically significant signal in the calibrated closure phases for J1407, and hence that it is single to within the detection limits of the observations. Using the same procedures as in our previous SAM work mentioned above (i.e., a Monte Carlo method that simulates random closure-phase data sets of a point source with closure-phase errors and covariances that match those of the real data), we found the contrast limits summarized in Fig. 2.

2.3 Direct imaging with Keck

J1407 was also observed with standard AO imaging immediately preceding the SAM observations, obtaining six integrations of 10 s in the K' filter. These observations used the narrow camera in full-frame mode (FOV=10 arcsec) and were obtained in a diagonal two-point dither pattern. We analysed each frame of imaging data using two complementary methods of PSF subtraction. For wide separations ($\rho > 600$ mas), where read noise dominated the error budget for companion detection, we subtracted an azimuthally smoothed median PSF. For small separations ($\rho \leq 600$ mas), where speckles from the primary star dominated the error budget, we searched the library of all single stars observed that night to find the best-fitting empirical template. We determined the best-fitting comparison star using the pixels at projected separations of $150 < \rho < 300$ mas, scaling each comparison star to the same total flux and then computing the reduced χ^2 of the fit. We then subtracted the best-fitting template star for each frame [implicitly a Locally Optimized Combination of Images (LOCI; Lafreniere et al. 2007) subtraction with $n = 1$ and globally optimized]. Finally, we stacked the residual frames and measured the standard deviation of fluxes measured through 4-pixel apertures in radial bins. We found no candidate companions in the stacked residuals that were more significant than 6σ, and hence we report a null detection with the 6σ detection limits shown in Fig. 2. The direct imaging limits at large radii reach down to 8 M_{Jup}, rising to 18 M_{Jup} at 26 au.

2.4 RV measurements with Magellan/MIKE

We obtained high-resolution spectra for J1407 on three consecutive nights starting on UT 2013 Feb 02 using the Magellan Inamori Kyocera Echelle (MIKE) optical echelle spectrograph on the Clay telescope at Magellan Observatory. We used the 0.7 arcsec slit, which yields spectral resolution of $R = 35\,000$ across a range of $\lambda = 3350$–9500 Å. The pixel scale oversamples the resolution with the 0.7 arcsec slit, so we observed with two times binning in the spatial and spectral directions to reduce readout overheads. The details of this observing campaign (such as selection of standards) can be found in Kraus et al. (2014).

We reduced the raw spectra using the CARPY pipeline (Kelson 2003).[1] In order to correct for residual wavelength errors (due to flexure and uneven slit illumination), we then cross-correlated the 7600 Å telluric A band for each spectrum against a well-exposed spectrum of a telluric standard, solving for the shift that places each spectrum into a common wavelength system defined by the atmosphere. Finally, we used the procedures described in Kraus et al. (2014) to estimate the spectral type and measure v_{rad}, $v \sin(i_\star)$, EW[Hα], and EW[Li$_{6708}$]. We adopt $v \sin(i_\star) = 14.6 \pm 0.4$ km s^{-1}, which we use later for a calculation of the minimum radius of the

[1] http://code.obs.carnegiescience.edu/mike

Table 4. MIKE observations of J1407.

Epoch (HJD)	t_{int} (s)	SNR @6600 Å	v_{rad} (km s^{-1})	$v \sin(i_\star)$ (km s^{-1})	SpT (km s^{-1})	EW[Hα] (Å)	EW[Li$_{6708}$] (Å)
56325.81	360	113	5.9 ± 0.3	14.9 ± 0.4	K4.8	−0.36	0.451
56326.84	720	164	5.5 ± 0.3	14.4 ± 0.4	K4.8	−0.23	0.441
56327.87	360	119	6.4 ± 0.3	14.6 ± 0.5	K4.8	−0.23	0.454

star J1407. In Table 4, we list the epochs and exposure times for our MIKE observations, the S/N measurement for each spectrum at 6600 Å, and the values measured from each spectrum.

2.5 RV measurements with CORALIE

J1407 was observed using the CORALIE spectrograph, mounted on to the 1.2 m Euler Telescope, installed at ESO's La Silla Observatory in Chile. This is a fibre-fed, thermally- stabilized, échelle spectrograph with a resolution ∼60 000. After a major upgrade in 2007 that improved its efficiency without comprising stability and precision, it has been routinely used in determining which of the candidate systems detected by SuperWASP are bona fide planets. Over seven years, it has detected over 100 transiting exoplanets (Wilson et al. 2008; Triaud et al. 2011; Hellier et al. 2014). J1407's brightness falls well within CORALIE's typical range of observation.

The spectra have been reduced using CORALIE's Data Reduction Software, which was built alongside those employed on High Accuracy Radial velocity Planet Searcher (HARPS), HARPS-South, and the Spectrographe pour l'Observation des Phénomènes des Intérieurs stellaires et des Exoplanètes (SOPHIE) and that have been shown to yield remarkable precision and accuracy (Dumusque et al. 2012; Molaro et al. 2013; Pepe et al. 2013). The spectra are wavelength-calibrated using a Thorium–Argon calibration lamp (Lovis & Pepe 2007). Each exposure is a simultaneous observation of the star and of a Th–Ar lamp. Calibration exposures throughout the night ensure that the instrumental drifts, mostly due to variations in pressure (for instance the solar-induced atmospheric tides), are corrected. The stellar spectra are cross-correlated using a weighted numerical K5-spectral mask, following the methods of Baranne et al. (1996). Radial velocities are computed from fitting a Gaussian profile on to the resulting cross-correlation function. Other parameters such as the span of the bisector slope and the full width at half-maximum (FWHM) of the cross-correlation function were measured as well. They provide good diagnostics for stellar activity (e.g. Queloz et al. 2001; Huélamo et al. 2008).

The first spectrum was obtained on UT 2013 May 30. It was a 3600 s exposure without simultaneous Th–Ar, to assess the observability of the target. We then follow the observing techniques devised in Dumusque et al. (2011) to mitigate stellar astrophysical noise: observations were scheduled by blocks of three spectra obtained on consecutive nights, to approximately match the rotation period of the star (Mamajek et al. 2012). 29 spectra with exposures ranging from 900 to 1800 s were obtained between UT 2013 June 30 and UT 2014 July 21 (Table 5). The observations in Fig. 3 show significant scatter in radial velocities, but also in the slope of the bisector (Fig. 4) and the width of the lines (Fig. 5). The variation in RV is strongly anti-correlated to the slope of the bisector, a sign that stellar activity is distorting the shape of absorption lines (see Fig. 6). The scatter in the bisector slope and FWHM has increased during the 2014 observing season compared to 2013.

The data were combined over each observing set, reducing the sample to nine individual measurements: the velocities were

Table 5. CORALIE observations of J1407.

BJD (d)	RV (km s^{-1})	σ_{RV} (km s^{-1})	FWHM (km s^{-1})	Bis_span (km s^{-1})	Exposure (s)
56442.576884	6.888	0.104	26.368	− 0.25	3600
56473.624422	6.929	0.094	27.590	0.09	1800
56474.551068	6.948	0.071	26.909	− 0.14	1800
56475.489472	7.056	0.081	26.836	− 0.33	1800
56506.514193	6.854	0.106	27.212	0.09	1800
56511.528147	6.698	0.063	26.709	0.04	1800
56514.557647	6.621	0.064	26.163	0.38	1800
56529.495203	7.386	0.114	26.741	− 0.42	1800
56532.532901	6.997	0.113	26.565	0.14	1800
56645.860211	8.089	0.053	28.932	− 2.87	1800
56646.848954	7.212	0.076	27.489	− 0.64	1223
56647.848845	6.630	0.078	27.834	0.76	1200
56687.864277	6.234	0.086	26.711	0.57	1200
56688.871105	7.144	0.073	26.836	− 0.43	1200
56689.832639	6.734	0.088	26.578	− 0.10	1200
56701.740155	7.121	0.088	27.115	− 0.65	1200
56702.733195	6.911	0.092	26.900	0.47	1200
56703.722404	6.599	0.103	27.955	1.68	1200
56745.690237	6.551	0.074	26.426	0.57	1200
56746.714550	7.033	0.076	27.455	− 0.33	1200
56747.718248	6.792	0.101	26.792	− 0.05	1200
56770.687959	6.347	0.103	27.126	0.28	900
56771.759089	6.925	0.102	26.855	− 0.65	900
56772.723642	6.896	0.092	26.486	− 0.08	900
56849.597842	6.583	0.131	27.345	− 1.13	900
56850.544421	7.490	0.150	28.263	0.63	900
56851.681482	7.734	0.129	28.548	0.54	900
56857.466766	6.378	0.077	26.468	0.27	900
56858.516701	7.202	0.092	27.411	− 0.71	900
56859.502439	7.664	0.125	27.681	1.74	900

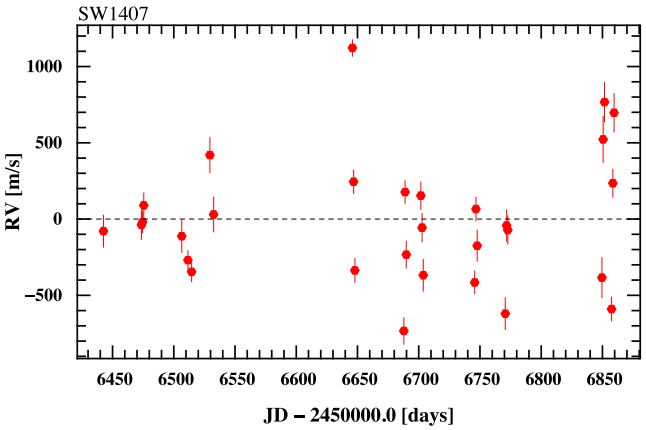

Figure 3. CORALIE measurements of the RV of J1407. The mean systemic velocity $\gamma = 6.91 \pm 0.04$ km s^{-1} has been subtracted off the data.

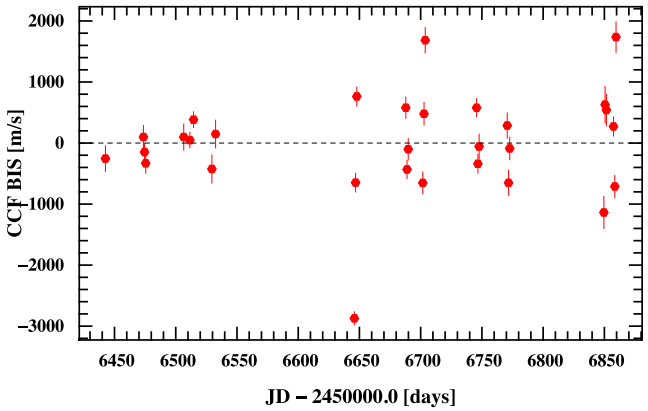

Figure 4. CORALIE measurements of the span in the slope of the bisector. The scatter has increased during the second season of observations. This is thought to be due to an increase in activity of the star.

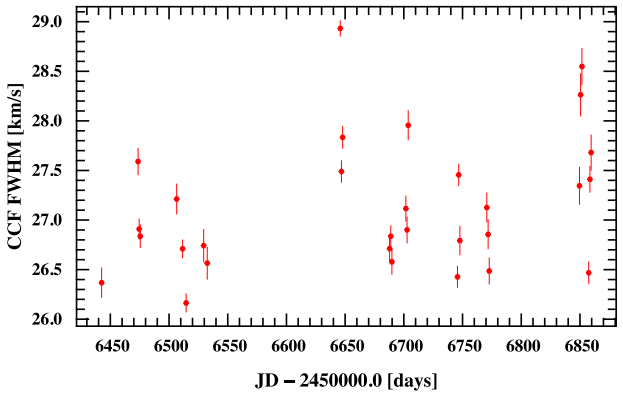

Figure 5. CORALIE measurements of the width (FWHM) of the cross-correlation function. The higher scatter in the second season is thought to be due to an increase in activity of the star.

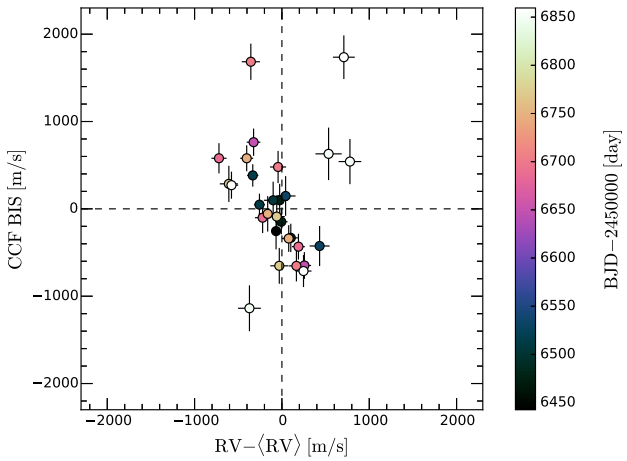

Figure 6. CORALIE measurements showing the span in the slope of the bisector plotted against the measured RV. Both quantities are anti-correlated, implying that the apparent RV variability is caused by a change in the shape of the cross-correlation function, implying that variation in the shapes of the lines are due to stellar activity.

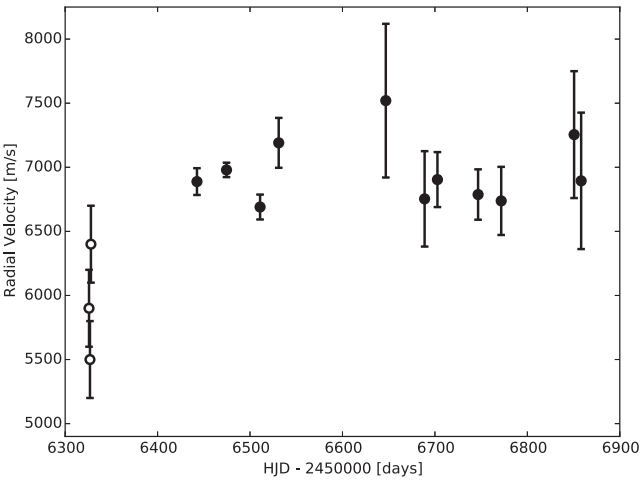

Figure 7. RV measurements of J1407. Open circles are data from MIKE and filled circles are binned data from CORALIE.

optimally averaged, with an associated error obtained from the rms within a set, and the corresponding mean date calculated. The results are graphically displayed in Fig. 7. Errors are larger in the seven epochs taken in the 2014 observing season, reflecting an increase in the activity of the star.

2.6 Photometric observations with PROMPT

The brightness of J1407 has been monitored nearly nightly between 2012 June and 2014 June, when possible, with the PROMPT-4 telescope at CTIO (Reichart et al. 2005). Three exposures of 3 s each are taken per clear night in both V and I filters. We report the V-band photometry in this contribution, which are sufficient to determine that no long eclipses have been seen during 330 epochs during the 2012–2014 observing seasons listed in Table 6. Three neighbouring comparison stars (listed in Table 7) have mean Johnson V magnitudes observed by the AAVSO Photometric All-Sky

Table 6. PROMPT 2012–2014 observing seasons.

Start epoch (HJD)	End epoch (HJD)	Dates
2456083	2456191	UT 2012 Jun 04–Sep 20
2456315	2456443	UT 2013 Jan 22–May 30
2456458	2456625	UT 2013 Jun 14–Nov 28
2456646	2456658	UT 2013 Dec 19–Dec 31
2456686	2456698	UT 2014 Jan 28–Feb 09
2456738	2456823	UT 2014 Mar 21–Jun 14

Table 7. J1407 and photometric comparison stars.

Name	2MASS	UCAC4	$V_{\rm mag}$
J1407	J14074792−3945427	252-062736	12.336 ± 0.034
S1	J14075890−3946482	252-062751	11.238 ± 0.016
S2	J14075952−3946151	252-062753	12.150 ± 0.017
S3	J14075199−3944151	252-062744	12.390 ± 0.024

Notes. 2MASS identifiers are from Skrutskie et al. (2006) and encode the ICRS position. UCAC4 star identifiers from Zacharias et al. (2013). Mean V magnitudes and uncertainties are from the AAVSO Photometric All-Sky Survey (APASS) Data Release 7. Long term monitoring of these stars with PROMPT-4 (330 epochs) shows that they are nearly constant at the <0.02 mag rms level.

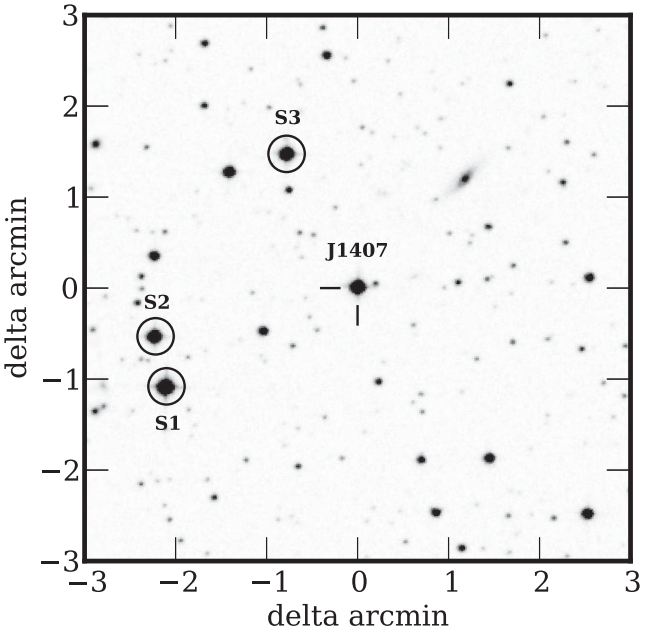

Figure 8. Finder chart for J1407 and three calibration stars generated using SkyView (2nd generation Digitized Sky Survey, red). North is up, east is left. Field of view is 6 by 6 arcmin.

Survey (APASS) accurate to ∼0.02 mag, and calibrated to Landolt fields (Data Release 7; Henden & Munari 2014). A finder chart for J1407 and the three comparison stars is provided in Fig. 8. From observations over 330 nights with PROMPT-4 during 2012–2014, we find that these comparison stars are photometrically quiet to <0.02 mag rms, and hence provide adequate comparison stars for assessing the variability of J1407. Fig. 9 shows the 2012 June to 2014 June *V*-band light curve for J1407 using calibrator star S1 for comparison. From comparison of J1407's brightness to the three APASS comparison stars, we find that the 2012–2014 average *V* magnitude for J1407 was $V = 12.365$, with a calibration-dominated uncertainty of ±0.02 mag. This compares well to the median *V* magnitudes estimated from previous time series photometry data sets (outside of eclipse): $V = 12.29$ (ASAS; Pojmanski 2002, 580 epochs), $V = 12.34$ (SuperWASP; Pollacco et al. 2006, 28 194 epochs, V_T converted to Johnson *V*), and $V = 12.34$ (APASS; Henden & Munari 2014, 8 epochs).

A sample of the photometry is shown in Table 8.

2.7 Photometric observations with ROAD

Nightly observations of J1407[2] have been taken at the ROAD (Hambsch 2012) observatory in Chile, using a commercially available CCD camera from Finger Lakes Instrumentation,[3] an FLI ML16803 CCD, The Microline (ML) line of CCD cameras is a lightweight camera design which can hold a variety of CCD chips. We used a full frame Kodak KAF-16803 image sensor together with the 40 cm Optimized Dall Kirkham *f*/6.8 telescope from Orion Optics UK[4] to give a field of view of nearly 48 arcmin × 48 arcmin, and the data were binned 3 × 3 for a plate scale of 2.09 arcsec pixel^{-1} to keep the amount of data to a reasonable value. The download speed was 8 MHz, the preamplifier gain 1.4 e$^-$/ADU. The camera was thermoelectrically cooled to a temperature of −25°C. All the measurements are made with a photometric *V* filter from Astrodon corporation. Dark and Flat frame correction is done in the CCD camera control program MAXIM/DL.[5]

Data reduction is done using software developed by P. de Ponthierre [6] based on comparison stars from the AAVSO sequence for J1407. 000−BKN−848 (RA 14^{h}08^{m}18^s.78, Dec. −39°49′54″.1, mag 12.051) is used as a reference star and 000−BKN−850 (RA 14^{h}07^{m}40^s.73, Dec. −39°38′53″.7, mag 13.102) as a comparison star. While no colour transformation was made, the median *V* magnitude of the observations (12.38; rms = 0.02 mag) is within 0.02 mag of the PROMPT observations, and hence can be considered sufficiently accurate to the other *V*-band observations for our eclipse search. The resultant photometry is seen in Fig. 9.

A sample of the photometry is shown in Table 9.

3 REVISED STELLAR PARAMETERS FOR J1407

We update the stellar parameters for J1407 and present them in Table 10, together with references.

3.1 Revised spectral energy distribution

A new spectral energy distribution (SED) for J1407 was constructed using the Virtual Observatory SED Analyzer (VOSA).[7] Photometry in 14 bands was used: *B*, *g*′, *r*′, and *i*′ from APASS DR7 (Henden & Munari 2014), *V* from Section 2.6, *I*, *J*, K_s from DENIS (Epchtein et al. 1997), *J*, *H*, K_S from 2MASS (Skrutskie et al. 2006), and the *W*1, *W*2, *W*3, *W*4 bands from All-WISE (Wright et al. 2010). BT-SETTL models (Allard, Homeier & Freytag 2012b) with solar metallicity over range log(*g*) = 4–5 and extinction range $A_V = 0$–0.3 were fit to the photometric data. The best-fit SED (plotted in Fig. 10) has $T_{\rm eff} = 4400$ K, log(*g*) = 4.0, [α/Fe] = 0.2, negligible extinction ($A_V = 0.00$). The $T_{\rm eff}$ inferred from the SED fit is consistent with previous estimates (Mamajek et al. 2012; van Werkhoven et al. 2014) and the spectral type estimate (K4.8) from the MIKE analysis (Section 2.4). The SED bolometric flux is $(5.974 \pm 0.020) \times 10^{-11}$ erg s cm^{-2}, or on the IAU scale an apparent bolometric magnitude of 11.577 ± 0.037 mag. At the revised kinematic distance of 133 ± 12 pc (van Werkhoven et al. 2014), the revised luminosity is $\log(L/L_\odot) = -0.478 \pm 0.077$ dex (with the uncertainty dominated by the distance uncertainty).

3.2 Stellar equatorial velocity, stellar radius, and inclination

We can place some further constraints on the size and inclination of the star J1407. Adopting $T_{\rm eff} = 4400 \pm 100$ K from the SED fitting (consistent with previous estimates), the updated luminosityconverts to a new stellar radius estimate of 0.99 ± 0.11 $R_\odot$. With the revised $T_{\rm eff}$ and radius, and a period of 3.21 ± 0.01 d (van Werkhoven et al. 2014), we predict the star's equatorial rotation velocity to be $v_{\rm eq} = 15.7 \pm 1.7$ km s^{-1}.

A lower limit to the stellar radius of J1407 can be estimated directly from the projected rotational velocity (Section 2.4) and the

[2] http://www.aavso.org/apass
[3] http://www.flicamera.com/
[4] http://www.orionoptics.co.uk/
[5] http://cyanogen.com/
[6] LESVEPHOTOMETRY software (http://www.dppobservatory.net/AstroPrograms/Software4VSObservers.php).
[7] http://svo2.cab.inta-csic.es/theory/vosa4/

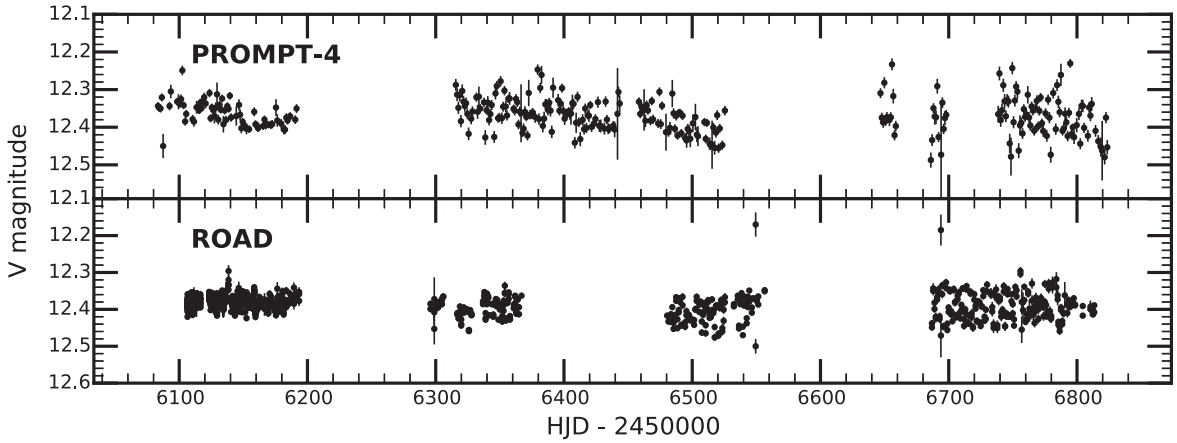

Figure 9. Photometry of J1407. Upper panel: PROMPT-4 *V*-band light curve for J1407 between 2012 June and 2014 June, covering 330 nights. Photometry has been measured with respect to calibration star S1 in Table 7. Lower panel: ROAD photometry of J1407 between 2012 July and 2014 June.

Table 8. A sample of the photometry from the PROMPT-4 telescope. The full table is available online.

Epoch (HJD – 2450000)	*V* band (mag)	*V*-band error (mag)
6083.46945	12.316	0.013
6084.46976	12.316	0.013
6085.48287	12.385	0.013
6086.46948	12.321	0.013
6087.46938	12.429	0.041

Table 9. A sample of the photometry from the ROAD observatory. The full table is available online.

Epoch (HJD)	V band (mag)	V band error (mag)
2456106.46175	12.387	0.008
2456106.46417	12.397	0.007
2456106.46658	12.394	0.007
2456106.46900	12.406	0.008
2456106.47142	12.396	0.007

Table 10. J1407 stellar parameters.

Parameter	Value	Notes
Mass	$0.9\,M_\odot$	van Werkhoven et al. (2014)
Radius	$0.99 \pm 0.11\,R_\odot$	This paper
Rotational period	3.21 ± 0.01 d	van Werkhoven et al. (2014)
Minimum radius	$R_\star > 0.93 \pm 0.02$	This paper
Distance	133 ± 12 pc	van Werkhoven et al. (2014)
$T_{\rm eff}$	4400 ± 100 K	This paper
$\log(L/L_\odot)$	-0.478 ± 0.077 dex	This paper

stellar rotation period. Taking $v \sin i_\star = 14.6 \pm 0.4\,{\rm km\,s^{-1}}$ and $P = 3.21 \pm 0.01$ d, we estimate a strong lower limit to the stellar radius of $R_\star > 0.93 \pm 0.02\,R_\odot$.

Since we have estimates of the equatorial and projected rotational velocities, we can estimate the inclination of the star J1407. We ran a Monte Carlo simulation taking into account the stellar parameters

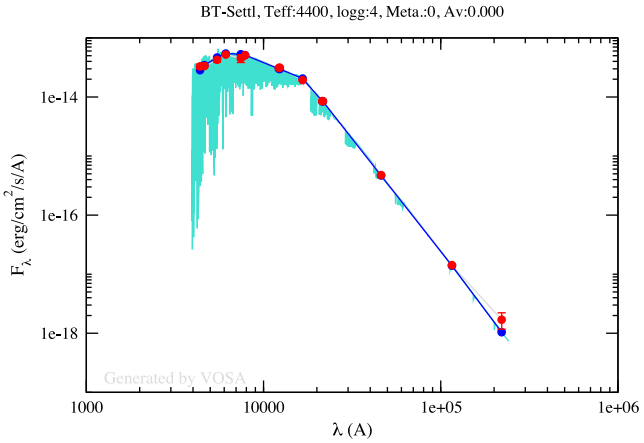

Figure 10. Spectral energy distribution and best-fitting model for J1407. Red points are the measured photometry with error bars. The dark blue points and line are the best fit of the model to the photometric points, and the light blue is the model spectrum.

and their uncertainties to estimate the probability distribution of the stellar inclination $i_\star$. For 10^6 simulations, 73.6 per cent resulted in physical solutions ($i_\star < 90^\circ$). We estimate the stellar inclination to be $i_\star = 63.9^\circ{}^{+10.5^\circ}_{-8.5^\circ}$ (68.3 per cent CL) or $^{+19.9^\circ}_{-15.0^\circ}$ (95.5 per cent CL).

4 ANALYSIS

We determine the constraints that these null detections provide by modelling orbits for J1407b as a function of orbital period. We assume that J1407b is gravitationally bound to J1407 and follows Keplerian orbits parametrized by orbital elements $a, e, i, P, T, \omega, \Omega$. The centre of the J1407b transit was UT 2007 April 27, and in the absence of any other perturbing bodies in the system, we assume that it follows a closed elliptical orbit with inclination $i = 90^\circ$ and ellipticity e.

We determine the mass and period limits for the case of circular orbits, and for the more generalized case of elliptical orbits in Section 4.2. For the total mass function of the system $M = 0.9\,M_\odot$ we investigate trial periods P from 2 to 1000 yr.

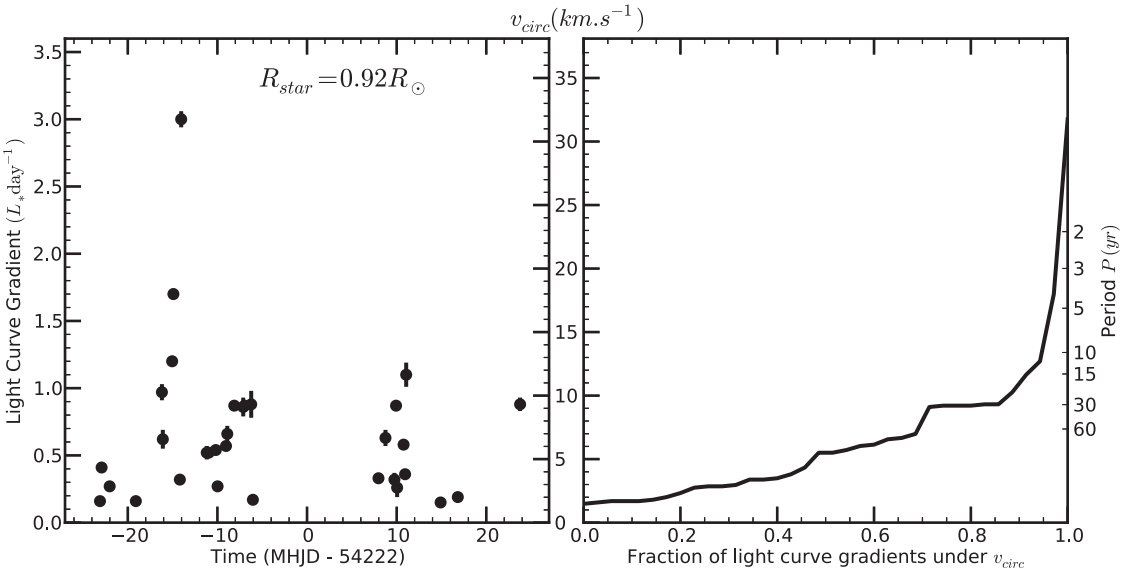

Figure 11. Gradients of the J1407 light curve as a function of time. The gradients are taken from van Werkhoven et al. (2014) and a stellar radius $R_* = 0.92\,R_\odot$ adopted. The right-hand scale shows the transverse velocity required to produce that gradient.

4.1 Circular orbits

4.1.1 Limits from ring geometry and orbital velocity for circular orbits

The companion is assumed to orbit J1407 with a circular orbital velocity $v_{\rm circ}$ which can bring a ring edge across the disc of the star, causing it to dim at a rate determined by the diameter of the star. In van Werkhoven et al. (2014), the light curve of J1407 is analysed and the minimum circular velocity required to match the observed gradients is determined. We recalculate the orbital velocities required for our determined minimum stellar radius from Section 3 and plot the results in Fig. 11 in the left-hand panel.

For increasing orbital period P, the circular orbital velocity becomes slower, and it is impossible to bring an opaque occulter across the disc of the star fast enough to explain the measured light-curve gradients seen in the J1407 data. The right-hand panel shows the fraction of measured gradients that can be explained by a dark or grey occulter moving a given circular orbital velocity, along with the corresponding orbital periods on the right-hand axis. It is clear, however, that decadal orbital periods are ruled out since they fail to explain many of the measured gradients. We consider that long-period solutions where the companion has orbital velocity $v_{\rm orb} < 12\,{\rm km\,s^{-1}}$ ($P \gtrsim 13.8$ yr; $a \gtrsim 5.5$ au) are strongly rejected by the presence of the steep light-curve gradients discussed in van Werkhoven et al. (2014).

4.1.2 Limits from direct imaging

We calculate the projected angular separation in arcseconds as a function of orbital period for the epochs of our two direct imaging observations UT 2013 March 27 and UT 2012 April 04, and these are plotted in Fig. 12 in panel (a). For an observation at a specific epoch, the projected angular separation varies as a function of trial period. The largest angular separation occurs when a putative companion reaches quadrature, and is zero when $\Delta t = nP/2$, where P is the period, n is a positive integer, and Δt is time between the epoch of observation and the mid-point of the eclipse, which we take to be UT 2007 April 29.

We do not detect any point sources in either epoch. The resultant sensitivity maps are in delta magnitudes, which when combined with the distance and age of the stellar system, are converted using BT-SETTL models (Allard et al. 2012a) into upper mass limits as a function of position on the sky. Azimuthally averaging these limits results in a contrast curve of upper companion mass versus distance from the J1407 in astronomical units (see Figs 1 and 2). Projected angular separation is then converted into companion upper mass limit in Fig. 12(b). The upper mass limits are indicated by a dotted line for the Keck image and a dashed line for the VLT image. The black region represents the upper mass limit from either Keck or VLT, whichever one gives the lower mass sensitivity at a given period.

4.1.3 Limits from photometric monitoring

J1407 underwent a series of nearly time-symmetric eclipse events with the mid-point of the eclipses on HJD 2454220 during early 2007. No other eclipses of J1407 are observed over the nine-year span of data from WASP-South and ASAS as reported in Mamajek et al. (2012), with a period search excluding all periods $P < 850$ d. The incompleteness of the photometry of J1407 is discussed in Mamajek et al. (2012) and presents orbital periods that are not ruled out by the photometric data.

In the new 2012–2014 time series photometry data from PROMPT-4 and ROAD, we see no new deep eclipses analogous to that seen in 2007. However, the recent PROMPT and ROAD photometric monitoring has helped rule out a wide range of periods of duration ∼4 to ∼7 yr. The most recent photometry is now excluding orbital periods that are a half and a third of the latest and most recent baselines, notably the window at 3.5 yr. Periods that are ruled out are represented by the dark grey vertical bars on the left-hand side of Fig. 12 in panels (a) and (b).

4.1.4 Limits from RV measurements

The RV measurements are shown in Fig. 7. These measurements are a combination of observations from both MIKE and CORALIE.

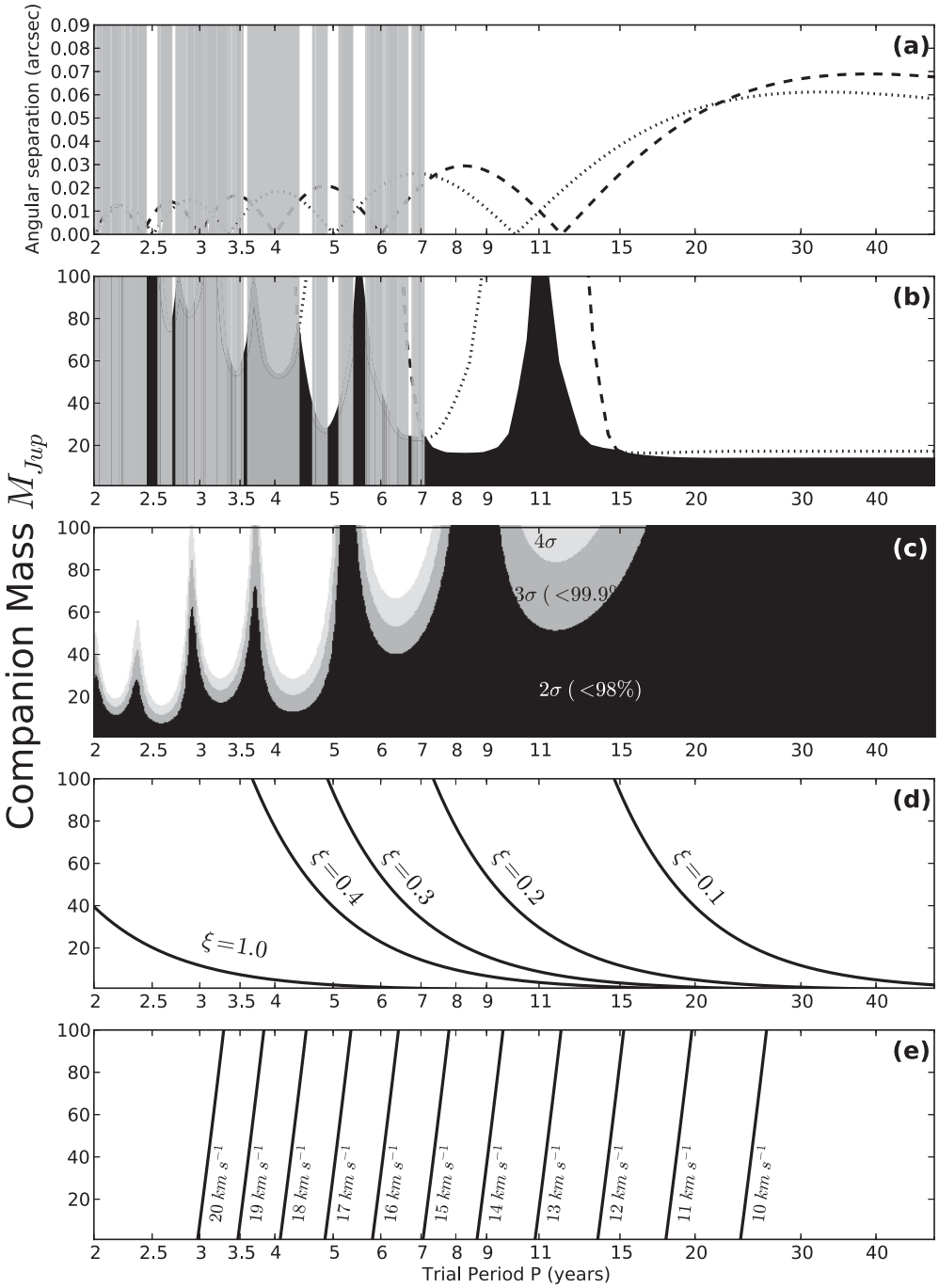

Figure 12. Limits to the period and mass of J1407b for circular orbits. Panel (a) shows projected angular separation as a function of orbital period P for J1407b for the Keck and VLT SAM imaging data assuming circular edge-on orbits with $r = 0$ at UT 2007 April 30. (b) Angular separation converted to upper mass limit. (c) Values of goodness of fit of the RV model expressed in standard deviations – black, dark grey, and light grey are 2σ, 3σ, 4σ respectively. Vertical grey bars are trial periods that have been ruled out by photometric monitoring. (d) Mass limits from Hill radius of the secondary companion and the duration of the eclipse. Panel (e) shows the circular orbital velocity $v_{\rm circ}$ of the companion relative to the primary.

The star is a rapid rotator as determined by photometric variability with a periodicity of 3.2 d (van Werkhoven et al. 2014). No known high-precision RV measurements of J1407 were taken at the time of the eclipse in 2007. We therefore construct an RV model $f(P, M)$ for J1407b using circular edge-on orbits, assuming a trial period P and secondary companion mass M to calculate the expected RVs at the epochs of observation $v_{\rm radial} = f(P, M) + C$, where C is constant offset that accounts for the unknown RV at the time of the 2007 transit. This model is then fit to the observed RVs with C as a free parameter that minimizes the χ^2 of the resultant model fit.

The MIKE observations have a time baseline of less than one week, and on their own do not produce significant constraints to our model. The combination of RV data from different telescopes with different instruments and RV data reduction pipelines introduces unknown systematic errors that are difficult to quantify. The

CORALIE data covers a baseline of over one year and typically has precision better than, or similar to, the MIKE data. The velocity zero-points should agree at the <200 m s^{-1} level, given the observed offsets seen between CORALIE velocities and those from the California Planet Search (those used in the MIKE analysis; e.g. Chubak et al. 2012). A larger effect is the velocity jitter introduced due to plage and star-spots, which could easily generate velocity variations at the tenths of km s^{-1} for a star rotating as fast as J1407 (e.g. Jeffers et al. 2014). By restricting our analysis to the CORALIE data, we do not need to consider the absolute calibration of the RV (expressed in the constant C in our model) nor the systematic offsets between the two instruments.

No significant RV variation is detected for the star. A fit to a horizontal line produces a reduced $\chi^2_r = 1.1 \pm 0.5$, and mean systemic velocity $\gamma = 6.91 \pm 0.04$ km s^{-1}. A slope produced a worse χ^2_r. At 95 per cent confidence, $|\dot{\gamma}| < 450$ m s^{-1} yr^{-1}. The CORALIE data alone excludes additional companions with masses $>12 M_{\rm Jup}$ on circular orbits shorter than one year (but longer than 3 d). The grid of $\chi^2_{\rm red}$ converted to goodness of fit in σ is shown in Fig. 12(c).

Using the Upper Cen–Lup (UCL) subgroup velocity vector from Chen et al. (2011, $U, V, W = -5.1 \pm 0.6, -19.7 \pm 0.4, -4.6 \pm 0.3$ km s^{-1}), we predict the RV of an ideal UCL member at the position of J1407 to be $\gamma = 7.0$ km s^{-1}, with a predicted rms scatter amongst members of ± 1.3 km s^{-1}. The measured RV is consistent with J1407's membership in the UCL subgroup of Sco–Cen, as proposed by Mamajek et al. (2012). Hence, the position, proper motion, excess lithium, strong X-ray emission, HR diagram position, and now RV, for J1407 are all consistent with UCL membership.

4.1.5 *Limits from dynamical constraints of the ring system*

The duration of the eclipse event in 2007 sets a dynamical constraint based on the stability of the ring system around J1407b. The longest transit time possible is one where the star J1407 passes through the middle of the disc and behind the secondary companion. The measured transit duration $t_{\rm d}$ therefore represents a lower limit on the total projected diameter of the ring system for non-zero impact parameters of primary star. Following the terminology of Mamajek et al. (2012), we define the radius of the disc system as measured from J1407b as $r_{\rm d}$. The radius where the gravity of J1407b is dominant over the primary star is defined as the Hill radius $r_{\rm H}$. Defining the ratio $\xi = r_{\rm d}/r_{\rm H}$ so that we can express the disc radius in terms of Hill radius, we can then calculate the expected ξ for a given orbital period and mass of J1407b.

The radius of the disc is related to the eclipse duration by

$$r_{\rm disc} = \pi a t_{\rm d} P^{-1}.$$

Taking $r_{\rm H} = a \left(\frac{M}{3M_*}\right)^1 /3$ and the mass of the companion J1407b as M we then have:

$$M = 3M_* \left(\frac{\pi t_{\rm d}}{\xi P}\right)^3.$$

M_* is the mass of the star J1407 'A', a is adopted semimajor axis (although we are assuming circular orbits), and P is the orbital period. Lines of ξ for values of 0.1, 0.2, 0.3, 0.4, and 1.0 are plotted in Fig. 12(d). A value of 1.0 represents a disc system completely filling the Hill sphere and presents an extreme upper limit on the potential minimum mass required for J1407b. Martin & Lubow (2011) suggest a tidal truncation limit of $\xi \sim 0.4$ and hydrodynamic simulations of planets in circumstellar discs find $\xi \sim 0.3$ (Quillen & Trilling 1998; Ayliffe & Bate 2009). For the Galilean satellites forming in the Jovian circumplanetary disc after dissipation, smaller values of $\xi \sim 0.1$–0.2 are found (Canup & Ward 2002; Magni & Coradini 2004; Ward & Canup 2010). Values of ξ may therefore range from 0.1 up to 1.0, with a more precise value determined by subsequent detection of the next eclipse. However, based on theoretical predictions, we consider $\xi > 0.4$ solutions exceedingly unlikely.

4.1.6 *Combined mass–period limits for J1407b for circular orbits*

Combining the four sets of constraints listed previously, we show our limits on the possible mass and orbital period for circular orbits of J1407b in Fig. 13. Possible periods and masses are indicated by shaded regions in the figure. Overplotted are different values for ξ, the size of the ring system in units of the Hill sphere. Values of $\xi > 1$ are unstable and are ruled out. Simulations indicate that $\xi > 0.4$ are unlikely and that typical values are expected to be in the range of $0.1 < \xi < 0.3$ (Quillen & Trilling 1998; Canup & Ward

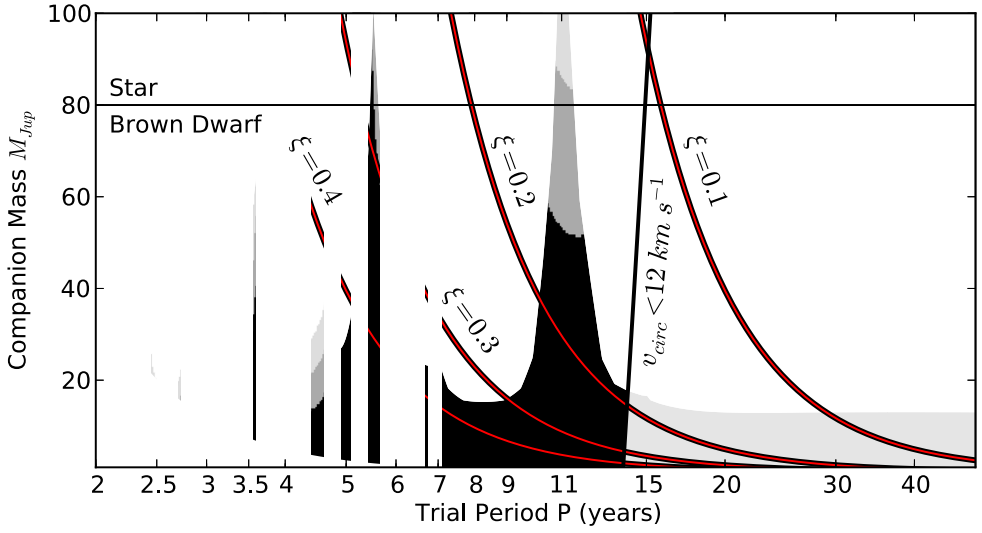

Figure 13. Combined mass/period limits for circular orbits of J1407b. This figure is a logical combination of the panels (b), (c), and (d) in Fig. 12.

Table 11. Probable mass of J1407b with circular orbits.

Mass range	$\xi < 1.0$	$\xi < 0.5$	$\xi < 0.4$	$\xi < 0.3$	$\xi < 0.2$
'star' $P(M > 80\,M_{\rm Jup})$	0.04 per cent	0.05 per cent	0.07 per cent	0.15 per cent	0.02 per cent
'brown dwarf' $P(13–80\,M_{\rm Jup})$	40 per cent	48 per cent	53 per cent	59 per cent	99 per cent
'planet' $P(< 13\,M_{\rm Jup})$	60 per cent	52 per cent	47 per cent	41 per cent	2 per cent
Probable period $\overline{P}$ (yr)	9.0	9.5	10.2	12.1	12.6
Probable mass $\overline{M}$ ($M_{\rm Jup}$)	13.6	15.6	17.1	16.1	26.1

2002; Magni & Coradini 2004; Ayliffe & Bate 2009; Ward & Canup 2010).

The figure shows that the mass of the secondary is substellar (below 80 $M_{\rm Jup}$ for solar composition; Saumon & Marley 2008)[8] for many periods, with the exception of a region of stellar mass at 5.5 and 11 yr. The RV measurements strongly constrain masses at 11 yr, but only slightly constrain at the 5.5 yr period. We can estimate the probability that the companion is above the deuterium burning limit by using the χ^2 fit from the RV model and the constraints from the non-detections of the measurements presented in this paper. We evaluate the χ^2 of the RV model fit for a linear sampling in companion mass from 1–100 $M_{\rm Jup}$, and a logarithmic sampling in period from 2–15 yr (corresponding to $v_{\rm circ} \approx 12\,{\rm km\,s^{-1}}$). The probability *Prob* at each sample point of mass and period is calculated using $Prob(M, P) \propto \exp(-\chi^2/2)$, and then we normalize $Prob(M, P)$ by summing over all masses and periods and setting this sum to unity.

By integrating this grid of probability over ranges of masses, we can determine how likely it will be that J1407b lies within a given mass range. Taking stellar ($M > 80\,M_{\rm Jup}$), brown dwarf ($80\,M_{\rm Jup} > M > 13\,M_{\rm Jup}$) and planetary ($M < 13\,M_{\rm Jup}$) masses and integrating over all periods, we calculate the normalized probabilities as listed in Table 11. We explore the probabilities for different values of the disc size in terms of Hill radius ξ. The probability that J1407b is a stellar mass object is less than 0.1 per cent for all values of ξ, corresponding to a 3.5σ likelihood. We can conclude that J1407b is therefore a substellar object. For all values of ξ greater than 0.3, J1407b is equally likely to be a brown dwarf or a planetary mass object.

4.2 Elliptical orbits

The light curve of J1407 shows rapid variation during the 2007 eclipse, and regardless of the detailed large-scale structure in orbit around J1407b, the largest gradients in the light curve imply a transverse velocity of $32\,{\rm km\,s^{-1}}$ for the occulting material. If the occulting material is in orbit around J1407b itself and is not azimuthally symmetric about J1407b then it is possible that the velocity of this clumped material vectorially adds with the orbital velocity of J1407b to produce the resultant transverse velocity that we see in the light curve – see van Werkhoven et al. (2014, section 6.2) for a discussion. Here, we explore the limiting case for elliptical orbit solutions to J1407b where the transverse velocity is entirely due to the orbital velocity of J1407b. Together with the circular case in the previous section, these two models then bracket the whole possible range of orbital solutions for J1407b.

[8] Saumon & Marley (2008) estimate the H-burning limit (defined by stars that stably fuse H at age 10 Gyr) as 0.075 $M_\odot$, or ~78.6$M_{\rm Jup}$. We simply adopt the rounded value 80 $M_{\rm Jup}$ as a conservative estimate of the H-burning limit.

4.2.1 Limits from ring geometry and orbital velocity for elliptical orbits

As seen in the previous section, there are no possible circular orbits that have a high-enough orbital velocity to explain the highest light-curve gradients. Instead, we will assume that all transverse velocity is due to orbital motion of J1407b at periastron, setting ω and Ω appropriately for periastron at primary transit.

The companion itself is assumed to cross in front of J1407 with a transverse velocity v which can bring a ring edge across the disc of the star, causing it to dim at a rate determined by the diameter of the star. In van Werkhoven et al. (2014), the light curve of J1407 is analysed and the minimum transverse velocity required to match the observed gradients is determined. We recalculate the transverse velocities required for our determined minimum stellar radius from Section 3 and plot the results in Fig. 11 in the left-hand panel. The largest transverse velocity required is $32 \pm 2\,{\rm km\,s^{-1}}$. The largest orbital velocity $v_{\rm peri}$ is at periastron:

$$v_{\rm peri} = \frac{2\pi a}{P}\left(\frac{1+e}{1-e}\right)^{1/2}$$

If we assume that periastron occurs during the transit of J1407b, we can then determine the minimum eccentricity required to attain a transverse velocity of $v_{\rm peri}$. For values of a and P with $v_{\rm peri}$ to $32 \pm 2\,{\rm km\,s^{-1}}$, the resultant lines of minimum eccentricities is seen in Fig. 14(a).

4.2.2 Limits from direct imaging for elliptical orbits

Using values of M, P, and e we calculate the expected angular separation of J1407b at the two epochs of direct imaging observations. The angular separation at the two epochs for each mass and period is then converted into a direct imaging minimum detectable mass. If this mass is greater than the companion mass M, then that specific mass M would have been detected at that period P. For a fixed period P, the companion mass is undetectable up to a critical mass, and any higher mass is then detectable. The upper mass limits of the two epochs of direct imaging are combined in a manner similar to Section 4.1.2, and the direct imaging limits for elliptical orbits is shown in panel (b) in Fig. 14. These mass limits are higher than those seen for circular orbits because we are assuming that these elliptical orbits are oriented with the semimajor axis pointing along the line of the sight to J1407. The projected angular separation of J1407b from the primary star is smaller than the separation for a circular orbit of the same orbital period, resulting in higher mass limits.

4.2.3 Limits from photometric monitoring for elliptical orbits

Photometric monitoring rules out any elliptical orbits with $e < 0.3$, and significantly limits orbital eccentricities with $e < 0.6$, as periods

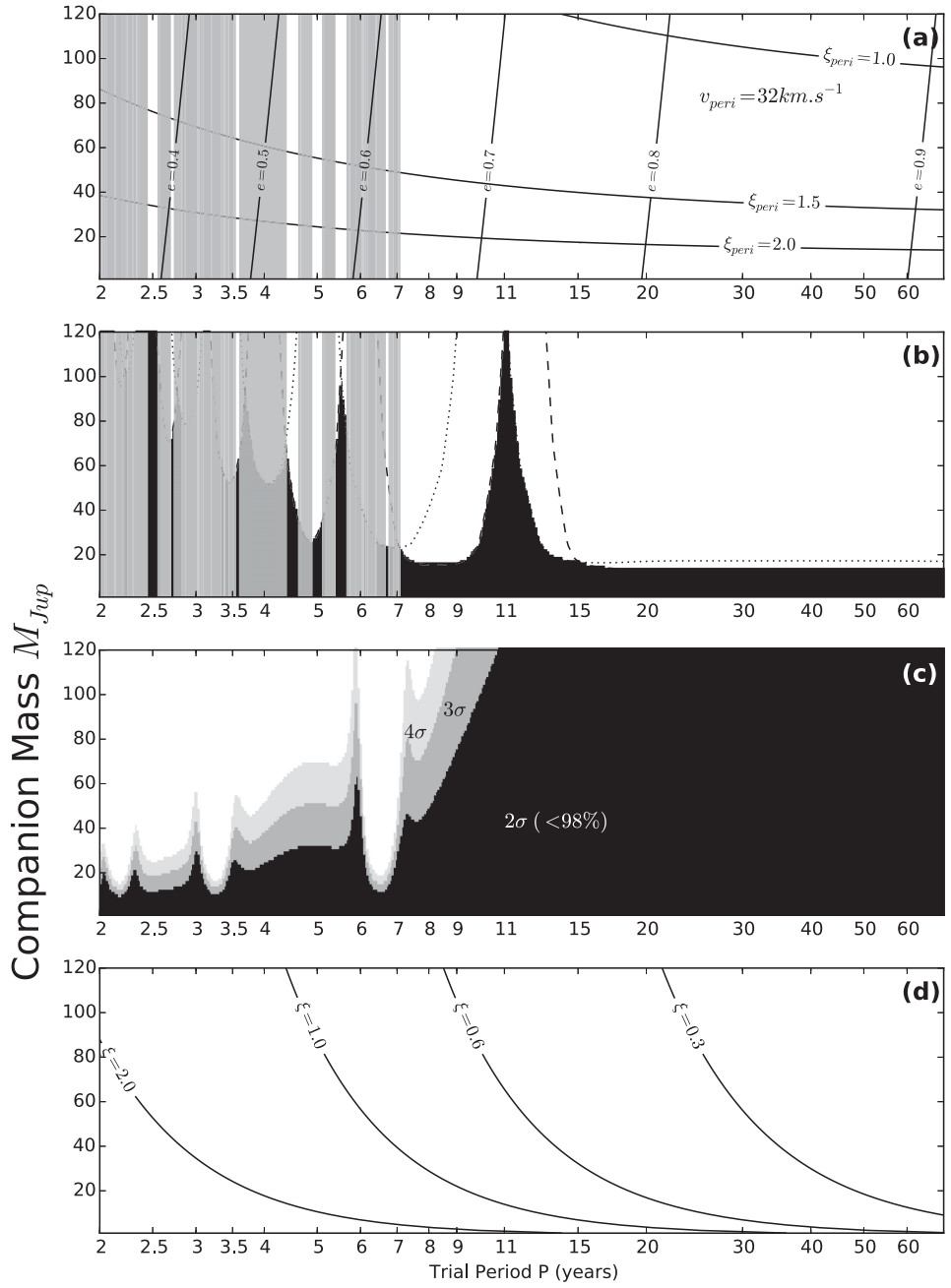

Figure 14. Limits to the period and mass of J1407b for elliptical orbits with periastron at the time of the eclipse in 2007. Vertical grey bars are trial periods that have been ruled out by photometric monitoring. (a) The minimum eccentricity of orbit required to get a periastron tangential velocity of 32 km s^{-1}. Diameter of the ring system in units of the Hill sphere at periastron are labelled with $\xi_{\rm peri}$. (b) Direct imaging limits from the two epochs of direct imaging. The black region indicates allowable values of mass M and period P. (c) Values of goodness of fit of the RV model expressed in standard deviations – black, dark grey, and light grey are 2σ, 3σ, 4σ respectively. (d) The diameter of the ring system in units of the Hill sphere calculated for the mean star/companion separation $a(1 + e^2/2)$.

shorter than 850 d are ruled completely out. Longer orbital periods therefore need more eccentric orbits to raise the periastron velocity to the 32 km s^{-1} required. This already presents a significant challenge as to how coherent dynamically long-lived structures can exist around a secondary companion.

4.2.4 Limits from RV measurements for elliptical orbits

We construct an RV model $f(P, M, e)$ for J1407b assuming periastron at the time of the 2007 transit, resulting in elliptical orbits with their semimajor axis pointing towards the earth. We carry out the same procedure as detailed in Section 4.1.4 for determining the fit for these elliptical orbits and the resultant χ^2 is converted to a probability as seen in Fig. 14(c).

4.2.5 Limits from the Hill sphere for elliptical orbits

For elliptical orbits, the Hill radius will change with time, reaching a minimum at periastron. Given the duration of the eclipse of 54 d, we calculate the size of the ring system at periastron in units of the Hill

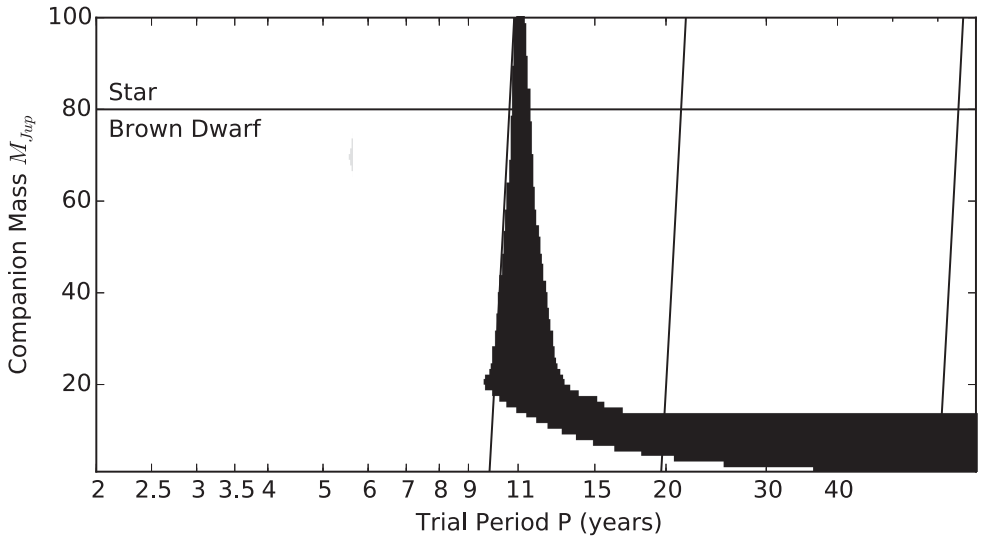

Figure 15. Combined mass/period limits for J1407b with elliptical orbits. This figure is a logical combination of the panels (b), (c), and (d) in Fig. 14. The three slanted lines represent eccentricities of 0.7, 0.8 and 0.9 from left to right respectively.

sphere $\xi_{\rm peri}$, and this is shown as the horizontal contours in panel (a) of Fig. 14. Periastron passage only comprises a small fraction of the total orbital period for very eccentric orbits, and the secondary companion will spend the majority of the orbital period at much larger separations. We therefore calculate the mean separation $\bar{a}$ which represents the separation averaged over one orbital period:

$$\bar{a} = a\left(1 + \frac{e^2}{2}\right).$$

The diameter of the ring system is calculated from $v_{\rm peri}$ and 54 d of eclipse, resulting in a larger ring diameter than for the equivalent circular orbit with period P. The diameter of ring system in units of the Hill sphere is shown in panel (d) of Fig. 14.

4.2.6 *Combined mass–period limits for J1407b for elliptical orbits*

Combining the four sets of constraints listed previously, we show our limits on the possible mass and orbital period for elliptical orbits of J1407b in Fig. 15. Possible periods and masses are indicated by shaded regions in the figure. Overplotted are different values for e.

The mass limits for the elliptical orbits are higher than for the circular orbits. This is a result of choosing elliptical orbits with the constraint of having periastron occur at the time of the eclipse in 2007 – orbits of a given period P have smaller semiminor axes compared to circular orbits, and so the projected angular separation is correspondingly smaller. This also increases the mass limits derived from the RV measurements. After passage through periastron, the secondary companion spends most of its orbit at distances larger than the semimajor axis, with correspondingly much smaller radial velocities seen in the star, and much smaller corresponding accelerations.

A minimum eccentricity of 0.5 is required to keep the ring system within the Hill sphere, although this is dependent on the precise nature of the interaction of the secondary on such an eccentric orbit with the surrounding ring system. Instead of limits due to gradient velocities (as considered for circular orbits), we are now limited by the eccentricity of the orbit of J1407b. Table 12 shows the relative probabilities for the eccentric orbital solutions, computed in a similar manner to Table 11. The most significant result is that

Table 12. Probable mass of J1407b for elliptical orbits.

Mass range	$e < 0.9$	$e < 0.8$
'star' $P(M > 80\,M_{\rm Jup})$	0.5 per cent	1.2 per cent
'brown dwarf' $P(13–80\,M_{\rm Jup})$	34 per cent	71 per cent
'planet' $P(< 13\,M_{\rm Jup})$	65 per cent	28 per cent
Probable period $\overline{P}$ (yr)	27.5	13.3
Probable mass $\overline{M}$ ($M_{\rm Jup}$)	14.0	23.8

J1407b requires a highly eccentric ($e > 0.7$) orbit. This is seen in other young stellar systems with low-mass companions – PZ Tel B is a brown dwarf mass companion with eccentricity greater than 0.6 (Biller et al. 2010; Mugrauer et al. 2012). A more critical constraint is that the ring system will overflow the Hill radius during the periastron passage, potentially highly perturbing the system and ring structure seen in the J1407 light curve. An analysis of the effects of a periastron passage on a giant ring system is beyond the current scope of this paper.

5 CONCLUSIONS

The observations reported here explore the highest angular resolutions attainable on single dish optical telescopes, along with contrasts that are not attainable with classical image subtraction techniques at small inner working angles. We can place strong constraints on the nature of the companion detected in transit in Mamajek et al. (2012) for circular orbits. Additional constraints based on high spectral resolution and precision RV measurements, combined with orbital periods ruled out by photometric monitoring and dynamical arguments show that J1407b is a substellar object and likely to be a planetary mass or brown dwarf mass object. Stability arguments favour longer periods where $\xi < 0.4$, whilst observations of rapid changes in the light curve over the course of a few hours (van Werkhoven et al. 2014) strongly suggest that the orbital period must be short ($P \lesssim 15$ yr). The ring system is also considerably larger than the Roche radius for the secondary companion, suggesting that we are seeing this ring system in a transitional state where exosatellites are in the process of formation.

Using elliptical orbital solutions to provide a large transverse velocity at periastron results in high orbital eccentricity solutions ($e > 0.7$), a large ring system that fills a significant fraction of the Hill sphere ($\xi > 0.5$) and an overflowing Hill sphere at periastron passage. These elliptical orbits provide significant challenges for ring structural stability, either requiring rapid dynamical settling within one orbital period or the stabilizing influence of exosatellites within the ring system.

All models imply a ring system for J1407b that fills at least 0.15 of the Hill sphere and is significantly larger than the Roche radius. These large rings are unstable on long time-scales and will ultimately accrete to form exosatellites, contrasting with Solar system models where moons are formed from gradual overflow over the Roche radius (Crida & Charnoz 2012).

For future observations, a detection of another eclipse is the most direct determination of the orbital period of J1407b. The observations presented in this paper will then give an upper and lower limit for the mass of the secondary companion and immediately constrain the nature of the system. Further RV observations will start to significantly rule out the largest masses at decade periods. An additional observation using SAM will also reduce the mass peaks at 5.5 and 11 yr periods.

Observations at longer wavelengths may be able to detect and possibly resolve the ring system around J1407b. Heating from the secondary companion combined with the large surface area of the ring system results in significant flux at submm wavelengths, detectable with the Atacama Large Millimeter Array (ALMA) or a large single dish submm telescope. When the full ALMA suite of telescopes is deployed, a high-precision astrometric detection can constrain the orbit of the secondary companion and measure the mass of the ring system.

Additional searches are now being carried out in archival photometric data to look for similar events that may have been overlooked or rejected by exoplanetary transit pipelines (e.g. Quillen et al. 2014). The ringed system around J1407b represents a unique laboratory to both spatially and spectrally resolve a young 16 Myr old disc around a likely substellar object and probe its structure to unprecedented spatial scales. Photometric monitoring is underway to look for the beginning of the next eclipse, and will signal the start of intensive observational campaigns over the subsequent weeks.

ACKNOWLEDGEMENTS

We are grateful to the VLT staff and to Nuria Huelamo who was vital in preparing these observations. Photometry from the PROMPT-4 telescope and the APASS was made possible by funding from the Robert Martin Ayers Science Fund. This research has made use of NASA's Astrophysics Data System and Skyview. This research has made use of the SIMBAD data base, operated at CDS, Strasbourg, France. Some of the observations were taken at the VLT (programme identifier 090.C-0827(A)). AHMJT received funding from the Swiss National Science Foundation in the form of an Advanced Mobility Post-doctoral Fellowship (P300P2-147773). SL acknowledges support by the French National Agency for Research (ANR-13-JS05-0005-01). EEM acknowledges support from NSF grants AST-1008908 and AST-1313029. This publication makes use of VOSA, developed under the Spanish Virtual Observatory project supported from the Spanish MICINN through grant AyA2011-24052. The Swiss, Euler Telescope is operated by the University of Geneva and is funded by the Swiss National Science Foundation. We thank the many observers that obtained CORALIE data on this target and appreciate the technical assistance that was provided by the Observatory of Geneva. We also thank the kind attention of the ESO staff at La Silla observatory. Some of the data presented herein were obtained at the W.M. Keck Observatory, which is operated as a scientific partnership among the California Institute of Technology, the University of California, and the National Aeronautics and Space Administration. The Observatory was made possible by the generous financial support of the W.M. Keck Foundation. The authors wish to recognize and acknowledge the very significant cultural role and reverence that the summit of Mauna Kea has always had within the indigenous Hawaiian community. We are most fortunate to have the opportunity to conduct observations from this mountain. All-WISE makes use of data from WISE, which is a joint project of the University of California, Los Angeles, and the Jet Propulsion Laboratory/California Institute of Technology, and NEOWISE, which is a project of the Jet Propulsion Laboratory/California Institute of Technology. WISE and NEOWISE are funded by the National Aeronautics and Space Administration. We thank the anonymous referee for their comments and suggestions on this paper.

REFERENCES

Allard F., Homeier D., Freytag B., 2012a, Phil. Trans. R. Soc. A, 370, 2765
Allard F., Homeier D., Freytag B., 2012b, in Johns-Krull C., Browning M. K., West A. A., eds, ASP Conf. Ser. Vol. 448, 16th Cambridge Workshop on Cool Stars, Stellar Systems, and the Sun, Astron. Soc. Pac., San Francisco, p. 91
Ayliffe B. A., Bate M. R., 2009, MNRAS, 397, 657
Baranne A. et al., 1996, A&AS, 119, 373
Biller B. A. et al., 2010, ApJ, 720, L82
Butters O. W. et al., 2010, A&A, 520, L10
Caffau E., Ludwig H.-G., Steffen M., Freytag B., Bonifacio P., 2011, Sol. Phys., 268, 255
Canup R. M., Ward W. R., 2002, AJ, 124, 3404
Chadima P. et al., 2011, A&A, 530, A146
Chen C. H., Mamajek E. E., Bitner M. A., Pecaut M., Su K. Y. L., Weinberger A. J., 2011, ApJ, 738, 122
Chubak C., Marcy G., Fischer D. A., Howard A. W., Isaacson H., Johnson J. A., Wright J. T., 2012, preprint (arXiv: e-prints)
Crida A., Charnoz S., 2012, Science, 338, 1196
Dumusque X., Udry S., Lovis C., Santos N. C., Monteiro M. J. P. F. G., 2011, A&A, 525, A140
Dumusque X. et al., 2012, Nature, 491, 207
Epchtein N. et al., 1997, ESO Messenger, 87, 27
Graczyk D., Mikołajewski M., Tomov T., Kolev D., Iliev I., 2003, A&A, 403, 1089
Guinan E. F., Dewarf L. E., 2002, in Tout C. A., van Hamme W., eds, ASP Conf. Ser. Vol. 279, Exotic Stars as Challenges to Evolution, Astron. Soc. Pac., San Francisco, p. 121
Hambsch F.-J., 2012, J. Am. Assoc. Var. Star Obs., 40, 1003
Hellier C. et al., 2014, MNRAS, 440, 1982
Henden A., Munari U., 2014, Contrib. Astron. Obs. Skalnate Pleso, 43, 518
Huélamo N. et al., 2008, A&A, 489, L9
Ireland M. J., Kraus A. L., 2008, ApJ, 678, L59
Ireland M. J., Kraus A., Martinache F., Lloyd J. P., Tuthill P. G., 2008, ApJ, 678, 463
Jeffers S. V., Barnes J. R., Jones H. R. A., Reiners A., Pinfield D. J., Marsden S. C., 2014, MNRAS, 438, 2717
Kelson D., 2003, PASP, 115, 688
Kloppenborg B. et al., 2010, Nature, 464, 870
Kraus A. L., Hillenbrand L. A., 2009, ApJ, 703, 1511
Kraus A. L., Ireland M. J., 2012, ApJ, 745, 5
Kraus A. L., Ireland M. J., Martinache F., Lloyd J. P., 2008, ApJ, 679, 762
Kraus A. L., Ireland M. J., Martinache F., Hillenbrand L. A., 2011, ApJ, 731, 8
Kraus A. L., Shkolnik E. L., Allers K. N., Liu M. C., 2014, AJ, 147, 146

Lacour S., Tuthill P., Amico P., Ireland M., Ehrenreich D., Huelamo N., Lagrange A.-M., 2011, A&A, 532, A72
Lafrenière D., Marois C., Doyon R., Nadeau D., Artigau E., 2007, ApJ, 660, 770
Le Bouquin J.-B., Absil O., 2012, A&A, 541, A89
Lovis C., Pepe F., 2007, A&A, 468, 1115
Magni G., Coradini A., 2004, Planet. Space Sci., 52, 343
Mamajek E. E., Quillen A. C., Pecaut M. J., Moolekamp F., Scott E. L., Kenworthy M. A., Collier Cameron A., Parley N. R., 2012, AJ, 143, 72
Martin R. G., Lubow S. H., 2011, MNRAS, 413, 1447
Mikolajewski M., Graczyk D., 1999, MNRAS, 303, 521
Mikolajewski M. et al., 2005, Ap&SS, 296, 445
Molaro P., Monaco L., Barbieri M., Zaggia S., 2013, MNRAS, 429, L79
Mugrauer M., Röll T., Ginski C., Vogt N., Neuhäuser R., Schmidt T. O. B., 2012, MNRAS, 424, 1714
Nakajima T., Kulkarni S. R., Gorham P. W., Ghez A. M., Neugebauer G., Oke J. B., Prince T. A., Readhead A. C. S., 1989, AJ, 97, 1510
Pecaut M. J., 2013, PhD thesis, Univ. Rochester
Pepe F. et al., 2013, Nature, 503, 377
Pojmanski G., 2002, Acta Astron., 52, 397
Pollacco D. L. et al., 2006, PASP, 118, 1407
Queloz D. et al., 2001, A&A, 379, 279
Quillen A. C., Trilling D. E., 1998, ApJ, 508, 707
Quillen A. C., Ciocca M., Carlin J. L., Bell C. P. M., Meng Z., 2014, MNRAS, 441, 2691
Reichart D. et al., 2005, Nuovo Cimento C, 28, 767
Saumon D., Marley M. S., 2008, ApJ, 689, 1327
Skrutskie M. F. et al., 2006, AJ, 131, 1163
Triaud A. H. M. J. et al., 2011, A&A, 531, A24
Tuthill P. et al., 2006, in Ellerbroek B. L., Calia D. B., eds, Proc. SPIE Conf. Ser. Vol. 6272, Advances in Adaptive Optics II. SPIE, Bellingham, p. 62723A
van Werkhoven T. I. M., Kenworthy M. A., Mamajek E. E., 2014, MNRAS, 441, 2845
Ward W. R., Canup R. M., 2010, AJ, 140, 1168
Wilson D. M. et al., 2008, ApJ, 675, L113
Winn J. N., Hamilton C. M., Herbst W. J., Hoffman J. L., Holman M. J., Johnson J. A., Kuchner M. J., 2006, ApJ, 644, 510
Wright E. L. et al., 2010, AJ, 140, 1868
Zacharias N., Finch C. T., Girard T. M., Henden A., Bartlett J. L., Monet D. G., Zacharias M. I., 2013, AJ, 145, 44

SUPPORTING INFORMATION

Additional Supporting Information may be found in the online version of this article:

Table 7. A sample of the photometry from the PROMPT-4 telescope.
Table 9. A sample of the photometry from the ROAD observatory (http://mnras.oxfordjournals.org/lookup/suppl/doi:10.1093/mnras/stu2067/-/DC1).

Please note: Oxford University Press is not responsible for the content or functionality of any supporting materials supplied by the authors. Any queries (other than missing material) should be directed to the corresponding author for the article.

This paper has been typeset from a TEX/LATEX file prepared by the author.